Supplementary material

Accessing the Free Expansion of a Crystalline Colloidal Drop by Optical Experiments.

Marcus Witt[1], G. H. Philipp Nguyen[2], Josefine R. von Puttkamer-Luerssen[1], Can Yilderim[1], Johannes A. B. Wagner[1], Ebrahim Malek[1,3], Sabrina Juretzka[1], Jorge L. Meyrelles Jr.[1,4], Maximilan Hofmann[1], Hartmut Löwen[4], and Thomas Palberg[1]

[1]Institute of Physics, Johannes Gutenberg University, Mainz, Germany

[2]Institute of Theoretical Physics II: Soft Matter, Heinrich-Heine-Universität Düsseldorf, Germany

[3]Institute for Biophysics, Goethe University Frankfurt, Germany

[4]Pontifícia Universidade Católica, Rio de Janeiro, Brazil

Supplementary video material

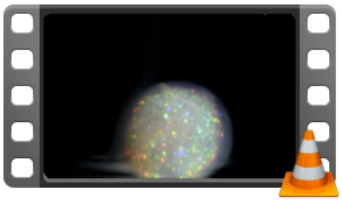

Video 1 WB.mp4

Video 1 Expansion of a spherical drop showing vivid Bragg scattering, as observed in white-light Bragg-mode (WB) under illumination with white light from the right. Time is shown in the upper right corner. The frame size is 5.1 mm × 5.1 mm.

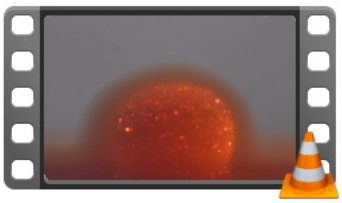

Video 2 MM 611 nm.mp4

Video 2 Expansion of a spherical drop showing Bragg single and multiple scattering, as observed in mixed mode (MM) under illumination with monochromatic light of λ = 611 nm from the right and diffuse white light from the back. Time is shown in the upper right corner. The frame size is 8 mm × 5 mm.

Particle characterization

Suspensions of exhaustively deionized and decarbonized suspensions were thoroughly characterized before use in this study [1, 2, 3, 4]. Figure S1a shows results from torsional resonance spectroscopy [2]. The shear modulus of the colloidal crystals is on the order of a few Pa. For comparison, the shear modulus of bcc iron is on the order of 10^{11} Pa. G increases with increasing density. The development

complies well with the expectations for a polycrystalline material of bcc crystal structure. The extracted charge is related to the effective Yukawa interaction strength. In Fig. S1b, we show the linear increase in background-corrected sample conductivity with increasing density. The extracted charge is related to the effective number of freely mobile counter-ions [1, 4]. Up to 100 μm^{-3} the sample structure could be determined by either static light scattering [5] or by reflection spectroscopy [6]. Exemplary results of the latter technique are shown in Fig. S2a. Bragg peaks are Miller-indexed for an assumed bcc structure. Note the significant increase in background scattering intensity at small wave-lengths, i.e. large q. It is due to incoherent multiple scattering, and its increase is in line with the expectation for Rayleigh scatterers [7]. The spectroscopic data are evaluated in Fig. S2b in a plot of q^2 versus $h^2+k^2+l^2$. Their arrangement on a straight line confirms the Miller-indexing of Fig. S2a. At larger densities, higher order reflections disappear in the MS-background. The positions of (200) and (211), however, keep evolving consistently with the nominally adjusted concentrations. Hence, we conclude the crystallite structure to be bcc even up to the largest investigated densities of ρ = 100 μm^{-3}.

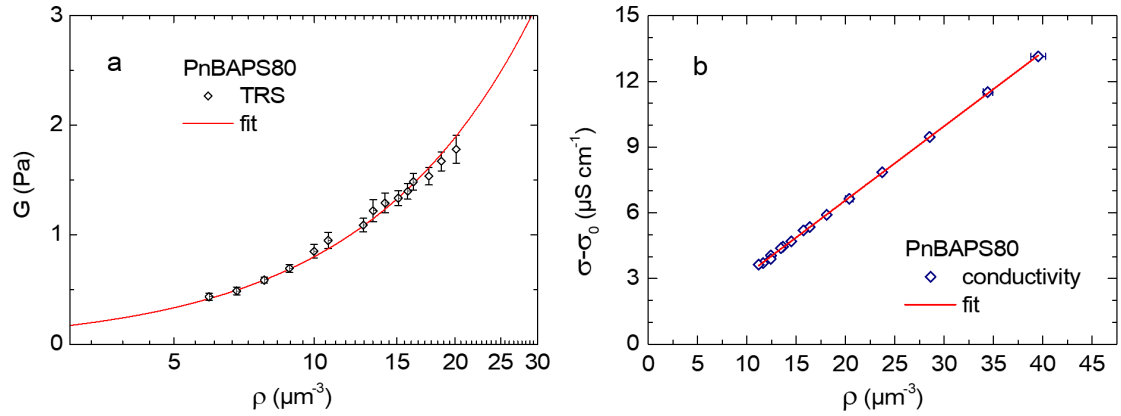

Fig. S1 Charge characterization of deionized and decarbonized suspensions of PnBAPS80. a) Shear modulus as determined from torsional resonance spectroscopy [2] in dependence on number density taken from static light scattering. The solid line is a two parameter least squares fit to the data with the n and the salt concentration from conductivity c = 0.2 $\mu molL^{-1}$. The fit returns Z_G = 365.1±2.3, where the error denotes the standard error at a confidence level of 0.95. b) Background-corrected conductivity in dependence on number density. The solid line is a two parameter least squares fit to the data using Hessinger's model of independent ion migration [1]. The fit returns Z = 513±3, where the error denotes the standard error at a confidence level of 0.95.

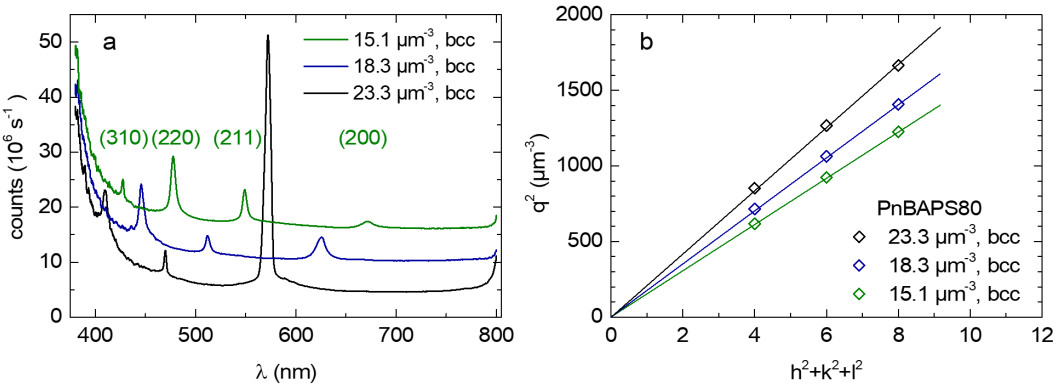

Fig. S2 Structure and density determination on deionized PnBAPS80. a) Miller indexed Debye-Scherrer scattering pattern from reflection spectroscopy for three different number densities indicated in the key. Curves are shifted for clarity. b) Plot of q^2 versus $h^2+k^2+l^2$. The solid lines are two-parameter least squares fits to the data using Bragg's formula and indexing the observed peaks for bcc crystal structure. From the slope, the fits return the ρ-values indicated in the key. The relative standard error at a confidence level of 0.95 is about 1.2%. At densities larger than 45 μm^{-3}, the scattering patterns displayed only two or even only one peak. This raised the relative error in density determination to about 2% and 4%, respectively.

For a known interaction effective charge, deionized conditions and increasing density, one may calculate the so-called state-lines [8] and compare them to the predictions of the phase behaviour of Yukawa particles. Following [9], it is convenient to do so in the plane of the effective temperature ($T_{\mathrm{eff}} = k_{\mathrm{B}}T/V(R)$ and the coupling parameter κR as shown in Fig. S3. In this plane, the sample will be fluid as long as its state point is above the melting line. Various authors have calculated the latter [10]. We here compare our state line to the results of Robbins et al. and of Meijer and Frenkel [9, 11]. The crystalline regime to the lower right shows in addition the location of the bcc-fcc transition expected to occur at elevated densities. The state lines reveal a shallow maximum under deionized conditions and a monotonous decrease of the effective temperature with increasing density at an underlying salt concentration of 6.3 $\mu molL^{-1}$. The experimentally probed densities are shown as small coloured symbols. We emphasize, that our experimental melting point agrees well with the predictions. The starting density is just inside the theoretically expected fcc region, but it is known from many other samples, that the bcc-fcc bulk transition is most often suppressed by kinetic effects such that only bcc is observed even at large κR [12]. Hence, we anticipate that we start in a bcc state. Note that during expansion, κ decreases by a factor of about 2 while T_{eff} decreases only very weakly.

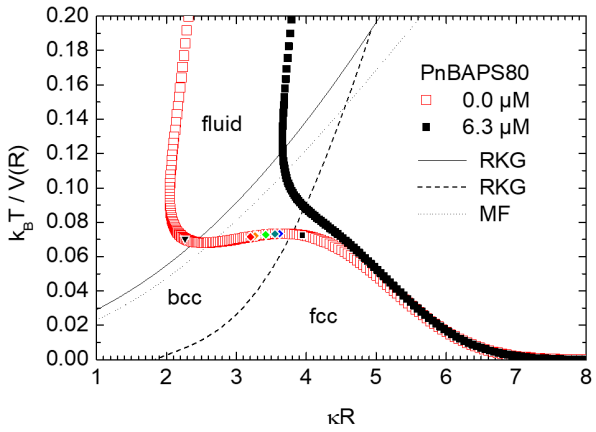

Fig. S3 State diagram and state lines of the PnBaPS80 particles in the effective temperature – coupling parameter plane. Data for the deionized and decarbonized state (red open diamonds) are compared to data at an electrolyte concentration of 6.3 $\mu molL^{-1}$. The small symbols denote the state points for the experimentally probed densities in the expanding crystalline droplets. The black triangle denotes the melting density, the black square denotes the start density. The coloured diamonds denote the densities as probed by monochromatic Bragg scattering at different wave lengths of 488 nm, 514 nm, 547 nm, 590 nm, 611 nm and 633 nm, corresponding to densities of 68.83 μm^{-3}, 58.91 μm^{-3}, 48.87 μm^{-3}, 38.95 μm^{-3}, and 31.54 μm^{-3}, respectively. The solid and dashed lines give the location of the melting line and the bcc-fcc transition, respectively, as predicted from simulations by Robbins et al. (RKG [9]); the dotted line shows the predictions of Meijer and Frenkel (MF [11]).

Additional details concerning the observation optics

Figure S4 shows an extended drawing of the optical arrangement used in the imaging experiments in top view with annotated comments. All elements are mounted on optical rails collinear with the optical axes (not shown), such that a facile rotation of the respective illumination and observation directions by 90° becomes possible. This turned out to be very useful for drop shape inspection.

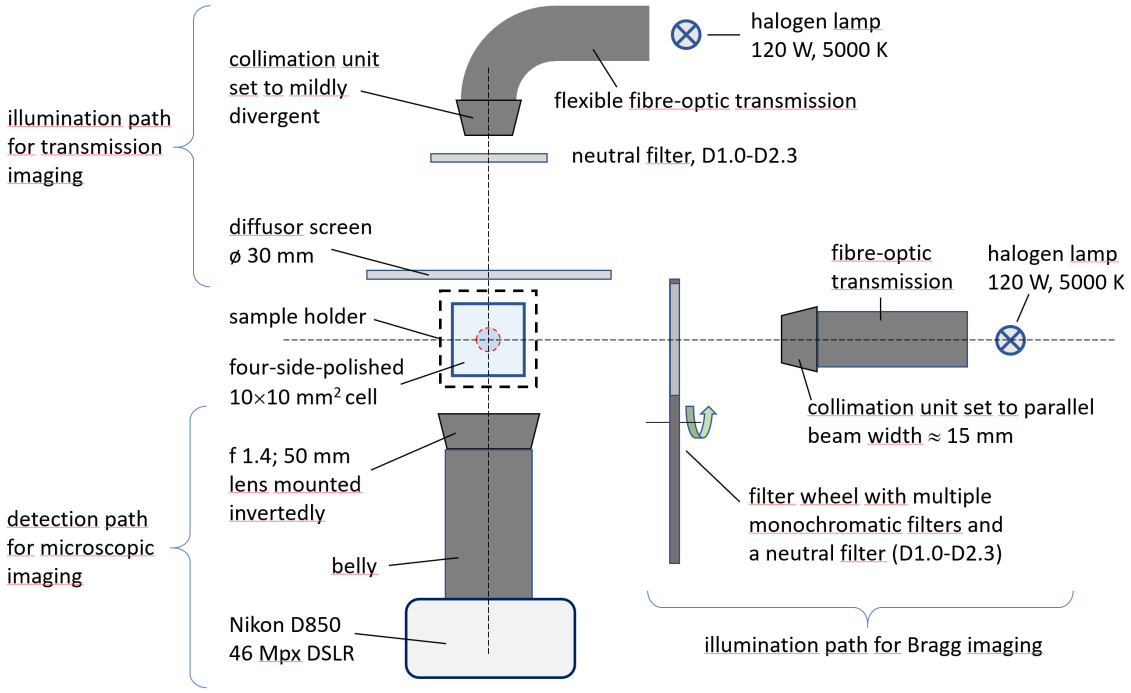

Fig. S4 more detailed optical set-up in top view. All items are labelled in this drawing. Commercial optical components used in illumination and observation are shown in dark grey. Additional optical elements for illumination adjustment are sketched in light grey. The vertical and the horizontal dashed lines indicate the optical axes of illumination and observation paths, which are oriented either at right angle to each other or collinearly.

Drop shapes

Drop compactness and shape are crucially influenced by the way the drops reach the observation position. Tip position with respect to the meniscus centre, fall height and the extrusion velocity crucially combine to determine the drop fate. Placing the drops off-centre with respect to the cell meniscus may lead to strong anisotropic distortions. Much too large fall heights lead to drop splitting, slightly larger than optimum fall height or fast extrusion promote doughnut-shapes. Too small fall heights result in drop adhesion to the top water surface. Some examples are shown in Fig. S4. With some practice, however, we regularly obtained compact, spheroidal or ellipsoidal drops. The following standard protocol was adapted for working in a 1cmx1cm cross-section cell: DI meniscus height 15mm, fall height 5-7mm as measured from the flat syringe needle tip to the water surface, slow extrusion and drop self-release by gravity. Quite reproducibly, this resulted in compact drops of prolate or oblate ellipsoidal shape, many of these being nearly spherical (Fig. S6b). We explicitly note, however, that irrespective of shape, the general free expansion and melting behaviour was well reproducible in all cases.

To further judge the shape, ellipsoidal candidates were inspected in either transmission or scattering also from the left direction in Fig. 1b, i.e. from 90° off the standard observation direction. Drops qualified for further evaluation when, upon inspection from both sides, the first eccentricity was below 0.14. This quantity was calculated using $\varepsilon = \sqrt{1 + a^2 / c^2}$ for the ellipsoids derived from fitting the projection of the MS-scattering surface by ellipses. In the examples of Fig. S6b the two rightmost drops qualified for further evaluation.

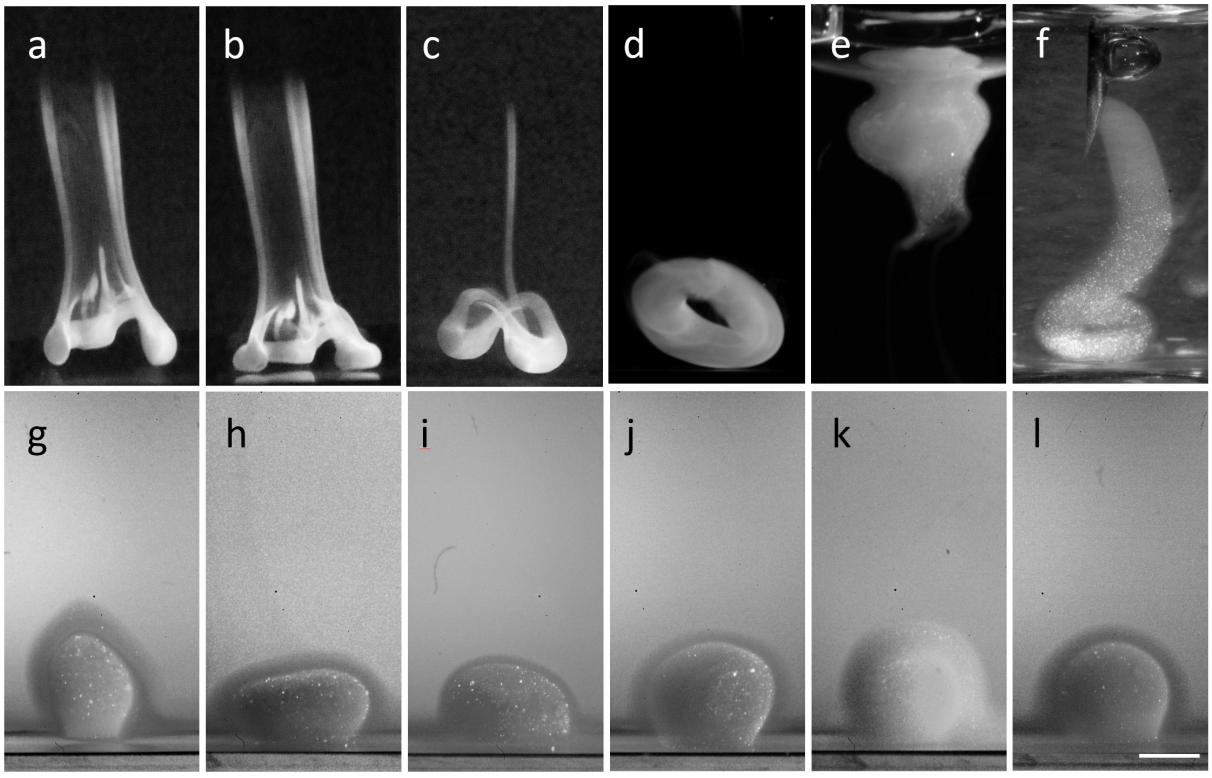

Fig. S5 Variation of drop shape. a) examples of drop shapes obtained under non-standard conditions. B/W renderings of WB images taken at very early times. a) and b) Much too large fall heights leads to drop splitting. Images were taken 1s apart just before and after touchdown. Note the easy deformation upon touchdown. c) and d) Too Large fall height leads to doughnut-shaped drops, which become more regular at decreasing fall height. e) Too small fall heights often result in substantial drop fractions adhering to the Water-air interface. f) extrusion with the needle tip inside the water produces wormlike shapes. g) to l) Drops produced by the standard extrusion procedure regularly show compact spheroidal shapes. B/W renderings of MM images taken at t ≈ 300 s. The scale bar is 2 mm. All drops appear to have a flat bottom. Shape determination was therefore performed on their upper hemisphere, not influenced by gravity and/or adjacent fluid sediment.

Very recently, we started experiments aiming at buoyancy-matched drops. To this end, the suspension was prepared from sugar solutions (analytical grade glucose, Merck, Germany) instead of DI-water. We checked, that subsequent deionization did not alter the suspension composition nor the particle properties. The final suspension had a mass density of ρ_{mass} = 1.005 gcm^{-3}. The same sugar concentration and density was adjusted in the receiving particle free solution. Experiments repeated with these ingredients regularly show buoyantly hovering, freely suspended drops, which as before expand and shrink. Drops appear more compact than before with significantly less suspension sheared off upon impact. However, most drop shapes were toroidal or mushroom-shaped. Two typical examples are shown in Fig. S5. Experiments aiming at spherical drops continue.

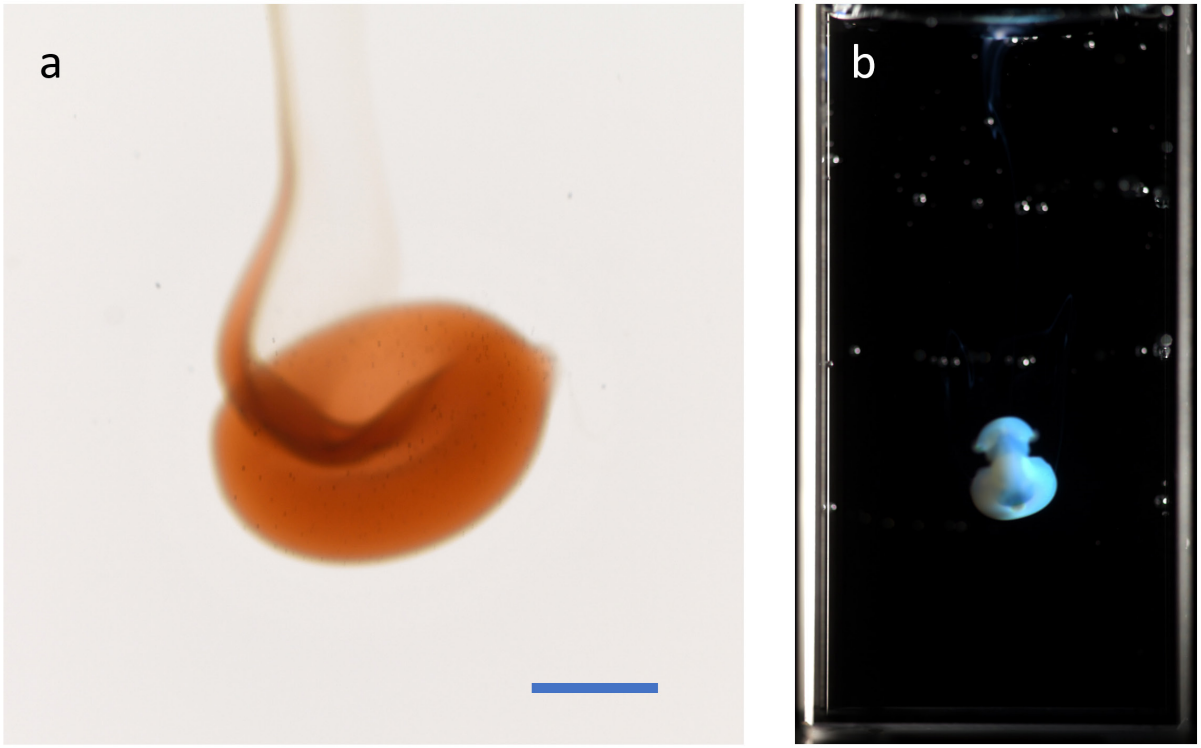

Fig. S6 Preliminary result from buoyancy-matching experiments. a) TR-image of a buoyant toroidal drop taken 20s after dropping. The scale bar is 2mm. b) WB-image taken 3 min after release of this freely suspended drop. Bath dimensions 10mm × 10 mm × 25mm.

Characterization of sample scattering properties

We characterized the scattering properties in separate experiments using transmission and reflection spectroscopy in slab geometry. The results of reflectometric structure analysis and number density calibration have been shown above. Since particles are non-absorbing, all extinction relies on scattering. Light is lost by both coherently and incoherently scattered light. Within Born approximation (single scattering), the intensity of *incoherently* scattered (IS) light is $I_{inc} \propto I_{f,0}\, n\, b(0)^2\, P(q)$. Here, the prefactor $I_{f,0}$ comprises the experimental details. It depends on the wavelength as λ^{-4} and on the distance between drop and sensor as R_D^2. $b(0)^2$ denotes the low q limit of the single particle scattering cross-section, n is the particle number density, $P(q) = b(q)^2/b(0)^2$ is the form factor. Incoherent scattering arises from size polydispersity [13, 14] and for the present small particles of PI = 0.08 a large incoherent scattering cross-section $b(0)^2\, P(q)$ is obtained at any angle. The *coherently* scattered intensity is $I_{coh} \propto I_{f,0}\, n\, b(0)^2\, P(q)\, S(q)$, where $S(q)$ is the structure factor [15] which depends on crystal structure and orientation. Figure S6a sketches the experimental scattering situation for bcc (110) with the illumination coming from the right and the outgoing beam impinging on the detector. In the present case of high densities, we have finely grained, polycrystalline samples showing a Debye-Scherrer scattering pattern in static light scattering and a multicoloured opalescence in WB imaging. Bcc crystals are stable for $\rho \geq \rho_m$ = 15 μm^{-3}. In the drop expansion experiments, they are observed at wavelengths of 488 nm $\leq \lambda \leq$ 633 nm and at Θ = 90°. Depending on density, different reflections contribute to recorded scattering (cf. Fig. S2a). The scattering vector of any Bragg reflection equals the reciprocal of a lattice plane spacing, $q = 2\pi/d_{hkl}$. For bcc crystals, the sum of Miller indices h,k,l is even and in the probed observation range we may only expect (110), (200) and (211) reflections. The first order reflection occurs at the MS-core surface. It is seen in MM images as a uniformly coloured

sphere (Fig. S6b), The second order appears in the enveloping region. The third order is visible only at the crystal sphere rim and shifts out of range for $n \geq 18.2\ \mu m^{-3}$ (Fig. S6c). By contrast, in transmission, all reflections in the range $0° < \Theta < 180°$ contribute to extinction.

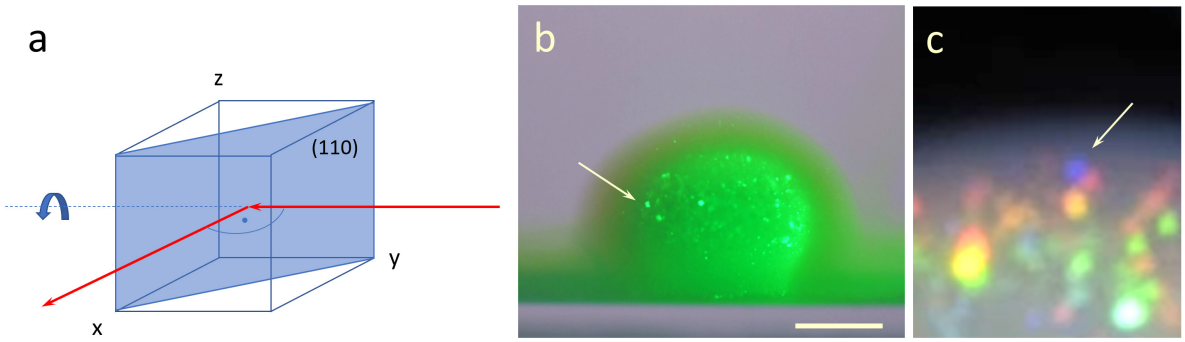

Fig. S7 Imaging details. a) Schematic drawing of a bcc crystal, suitably oriented of for (110) scattering at 90° towards the detector. Note that $\vec{k}_f$ lies within the locally flat isopycnic plane. By turning the crystal about the illumination optical axis, it can scatter in any direction within this plane and illuminate further material. b) MM observation of the multiply scattering (110) Bragg shell at $\lambda = 547$ nm corresponding to $\rho_C = 48.88\ \mu m^{-3}$. The arrow highlights a reflection occurring on the backside of the drop, which is not illuminated directly. The scale bar is 2 mm. c) Cropped WB image showing a blueish (211) Bragg reflection marked by the arrow. Only very occasionally, and only at rather early times, such 3rd order Bragg reflections are observed at the very rim of the crystal phase.

With increasing density, Born's approximation is invalidated, and we encounter weak to strong multiple scattering (MS) for both coherently and incoherently scattered light. MS has been studied in samples of homogeneous density and is generally considered detrimental for static and dynamic light scattering as well as for image analysis. Much effort has therefore been devoted to the isolation of the single scattering signal [16], but only few studies actually exploit its properties by sophisticated instrumentation. To characterize the general scattering and transmission characteristics for later use in the analysis of our main experiment, we performed white light transmission (TR) experiments in slab geometry. We placed a layer of concentrated suspension at the bottom of a rectangular cell of cross-section 5 mm × 2 mm and left it to expand uniaxially against the supernatant DI-water. During expansion, we recorded the transmitted light with a DSLR consumer camera. The deposited suspension expanded very slowly. Uniaxial expansion in slab geometry corresponds in principle to the free drop expansion studied in the main experiments. However, the influence of gravity and sample wall interactions severely influences the expansion dynamics in slab geometry and the resulting expansion dynamics should not be directly compared to the free expansion experiments.

A key feature of the slab geometry is that projection effects are avoided. We could access the wavelength dependent transmission of light in a more dilute sample as well as the relative contribution of different scattering mechanisms in different regions in a concentrated one. In Figure S7a, we show transmission profiles obtained at t = 1400 s in a fluid ordered sample with a starting density of $\rho = 20\ \mu m^{-3}$. We compare total transmission to the individual readings of the RGB channels. The observed dependence on wavelength demonstrates the expected λ^{-4} dependence of the prefactor $I_{f,0}$. Note, however, that due to the restricted wavelength resolution of the RGB channels the profiles obtained under white-light illumination are not strictly single exponential as would be expected from a Beer Lambert law and as indeed observed under monochromatic illumination [17, 18].

In Fig. S7b, we studied a sample with starting density ρ_0 = 110 µm^{-3}, which evolved layers of different structure and optical properties. We here set the illumination to maximum intensity. This leads to sensor saturation already at weak to moderate extinction (region labelled ⑤) but yields a detailed profile at larger extinction. The arrow marks the melting transition, located between regions ④ (fluid) and ③ (crystalline). Note the change in slope of the extinction curve. Above the crystalline/fluid transition, both scattering types contribute. However, with rapidly radially decreasing ρ and the simultaneous loss of fluid structure, a radial dependence of the transmitted light results which is more pronounced than in the crystalline region. Below the transition, extinction is mainly due to incoherent scattering and only little due to individual crystallites favourably oriented for (200) Bragg scattering. Thus, we observe a change in slope. Note further the small z-extension of the (200) Bragg scattering region ③ in these uniaxial expansion experiments, presumably due to gravitational compression by the fluid layer on top. Just below this region, we observe a deep transmission minimum denoted ②. In visual inspection of samples illuminated from the right by white light, its height correlates well with that of a narrow but vividly scattering horizontal feature showing an RGB colour-banding with red at its top. We attribute the transmission minimum to coherent MS due to strong 110 Bragg scattering occurring in layers of suitable density.

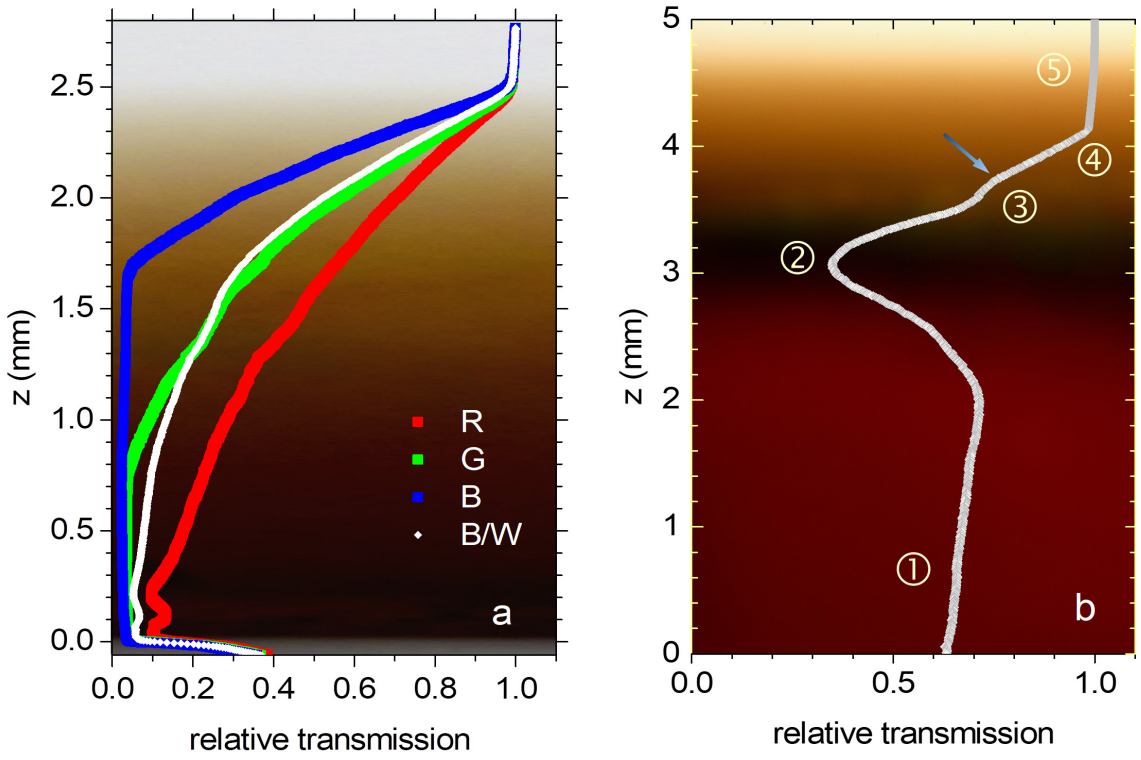

Fig. S8 Transmission experiments in slab geometry. In both panels, the background shows the original TR images. a) Relative transmission profiles obtained at t = 1400s in a fluid ordered sample with a starting density of ρ_0 = 20 µm^{-3}. We compare total transmission to the individual readings of the RGB channels. Note the pronounced increase of extinction with decreasing wavelength. b) Transmittance profile as a function of height above ground. The numbers mark regions with distinct characteristic developments of the relative transmission with height above ground. ①: moderately transparent bottom region with linearly rising transmittance, ②: MS extinction band; ③: continuation of the moderate extinction at a slightly increased level due to additional 2nd order Bragg scattering crystals; Note the sheet of crystallites in this narrow region faintly visible in the background image; ④: steeply

decreasing extinction in the fluid region. The border between ③ and ④ is marked by the grey arrow. The flattening of the transmittance curve beyond Z = 4 mm (region ⑤) is an artifact due to sensor saturation. For further details, see text.

Note that this coherent mechanism is self-restricting in the sense, that photons may propagate horizontally within the layer under continuing coherent scattering. Photons scattered into other regions, where the Bragg condition is not fulfilled any more, may there only scatter incoherently. In the drop expansion experiments, MS light propagation occurs in an analogous way within the spherical isopycnic shell. This can be illustrated using Fig. S6a. If the sketched crystal is rotated about the optical axis of the incoming beam, the resulting 90° Debye-Scherrer cone lies exactly within the locally flat isopycnic plane. In fact, Bragg scattered light can propagate throughout this plane and give rise to further reflections at suitably oriented crystallites. This wavelength- and density-dependent coherent MS is enhanced in particular at early stages of drop expansion, when crystallite sizes are still small, and the Bragg reflections show some Scherrer broadening [19]. This enables secondary scattering events also at less accurately oriented crystals and facilitates MS-light propagation within the whole of the shell up to the occurrence of Bragg reflections also within the core-shade. This is highlighted in Fig. S6b by the arrow in the shown MM-image recorded under illumination with light of λ = 548 nm. In WB images, this light propagation leads to the occurrence of concentric coloured bands and regions of near equal brightness on the right and left side of the drop centre (cf. Fig. 2e and Video 1). Overall, MS thus enhances imaging contrast and allows crystal sphere sizing as well as density profiling in the drop interior.

Coming back to the extinction experiments in Fig. 5b, the locally increased photon density within the MS-layer will, however, also result in a significant increase of incoherent scattering from within the layer and in its vicinity. Thus, in extinction, the width of the transmission minimum appears enhanced as compared to direct visual inspection. This effect is well-known as blurring in optical microscopy on turbid samples [**Fehler! Textmarke nicht definiert.**], and in the main scattering experiment, it affects spatial resolution in particular at short wavelengths. Finally, in the bottom region ①, the crystal lattice constant is too small to give rise to any Bragg scattering. Consequently, this region is again moderately transparent. Extinction occurs solely due to incoherent MS, and the transmission decreases nearly linearly with decreasing z.

Summarizing: the white light transmission experiments clearly demonstrate that a) 110 Bragg scattering causes pronounced extinction confined to a narrow band of specific density, which will narrow further under single wavelength illumination; b) a characteristic change of slope is associated with the melting transition; and c) throughout the crystalline core region we have only moderate extinction by incoherently light. These findings imply that: i) the core region of the drop is inaccessible to WB and MM imaging; ii) in TR images, we can determine the location of the melting transition from the change in radial slope of transmittance; iii) in MM images, the vivid 110 scattering seen for different wavelengths is in fact originating from thin ellipsoidal shells of constant density. Monitoring their wavelength- and time-dependent location will then allow for time-dependent density profiling.

Additional series of processed WB and MM images

For illustration purposes, Fig. S8 shows three additional time series taken in WB and MM mode. In these MM images, the drop is monochromatically illuminated from the right and simultaneously

from the back. Note the excellent visibility of (200) reflections in the broadening, more transparent outer regions of the crystal sphere in Figs. S8 c-h. Note further the gradual coarsening of the core structure. This is also seen clearly in Fig. S8 i-q and r-y. In both modes, we observe (110)-scattering also occurring from the “backside” of the sphere, which is not directly illuminated (e.g. Fig S8e, f, k and u). This nicely illustrates MS light propagation within the respective (110) shells. The images in the two MM series were recorded directly after one another. Note that some (but not all) individual reflections are visible in both corresponding colour panels. This indicates a radial density inhomogeneity within individual crystals.

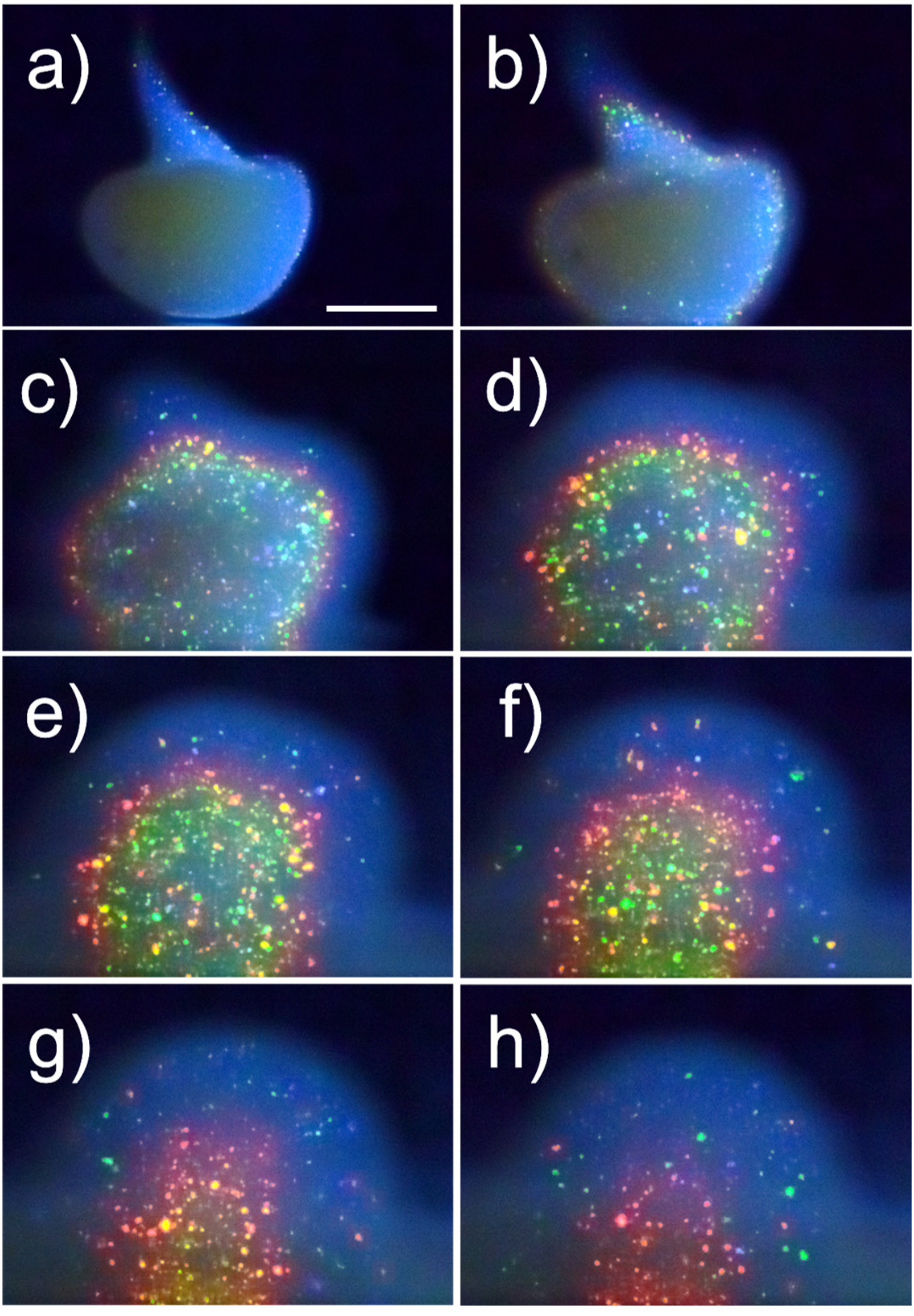
a)
b)
c)
d)
e)
f)
g)
h)

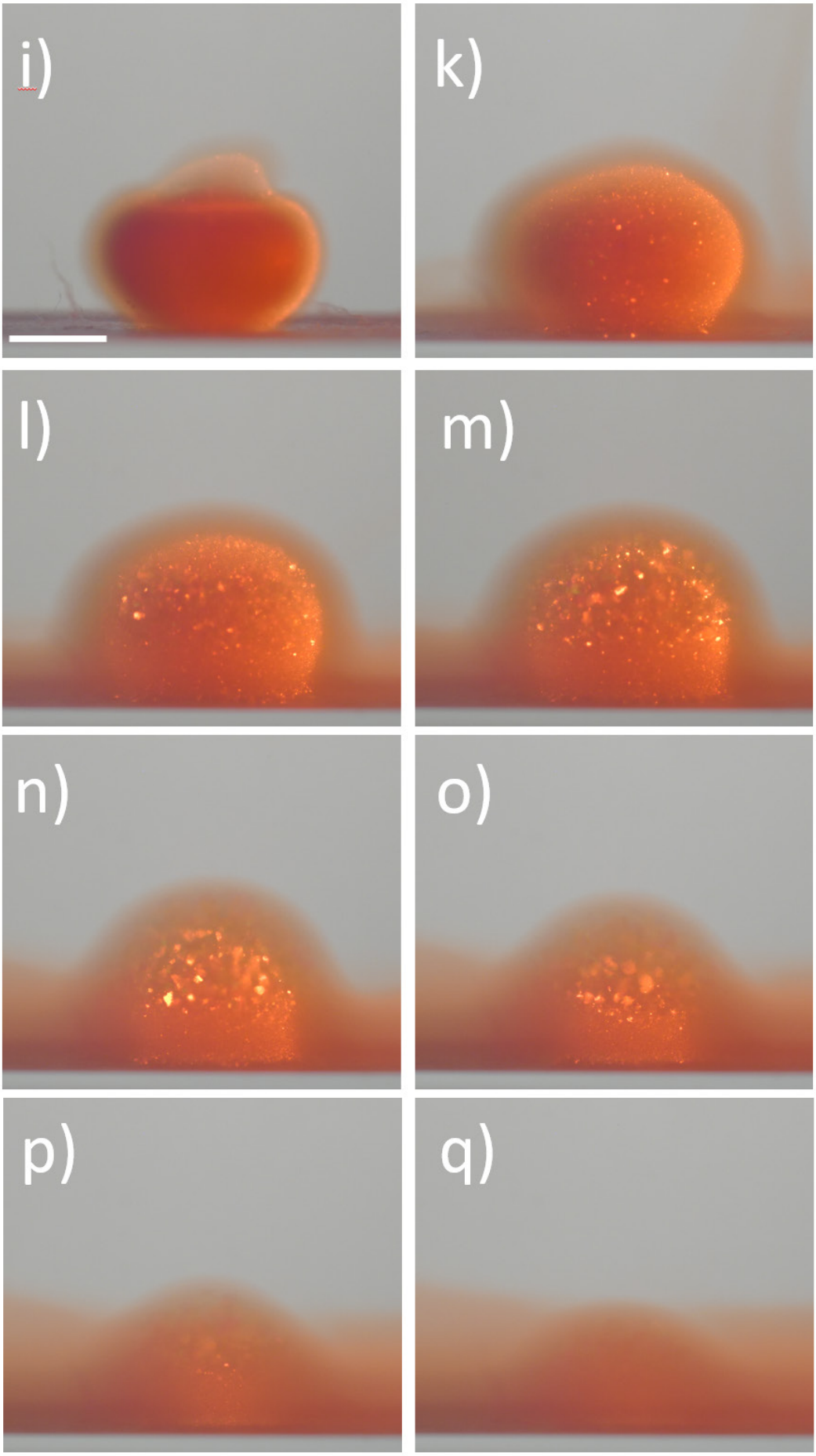
i)
k)
l)
m)
n)
o)
p)
q)

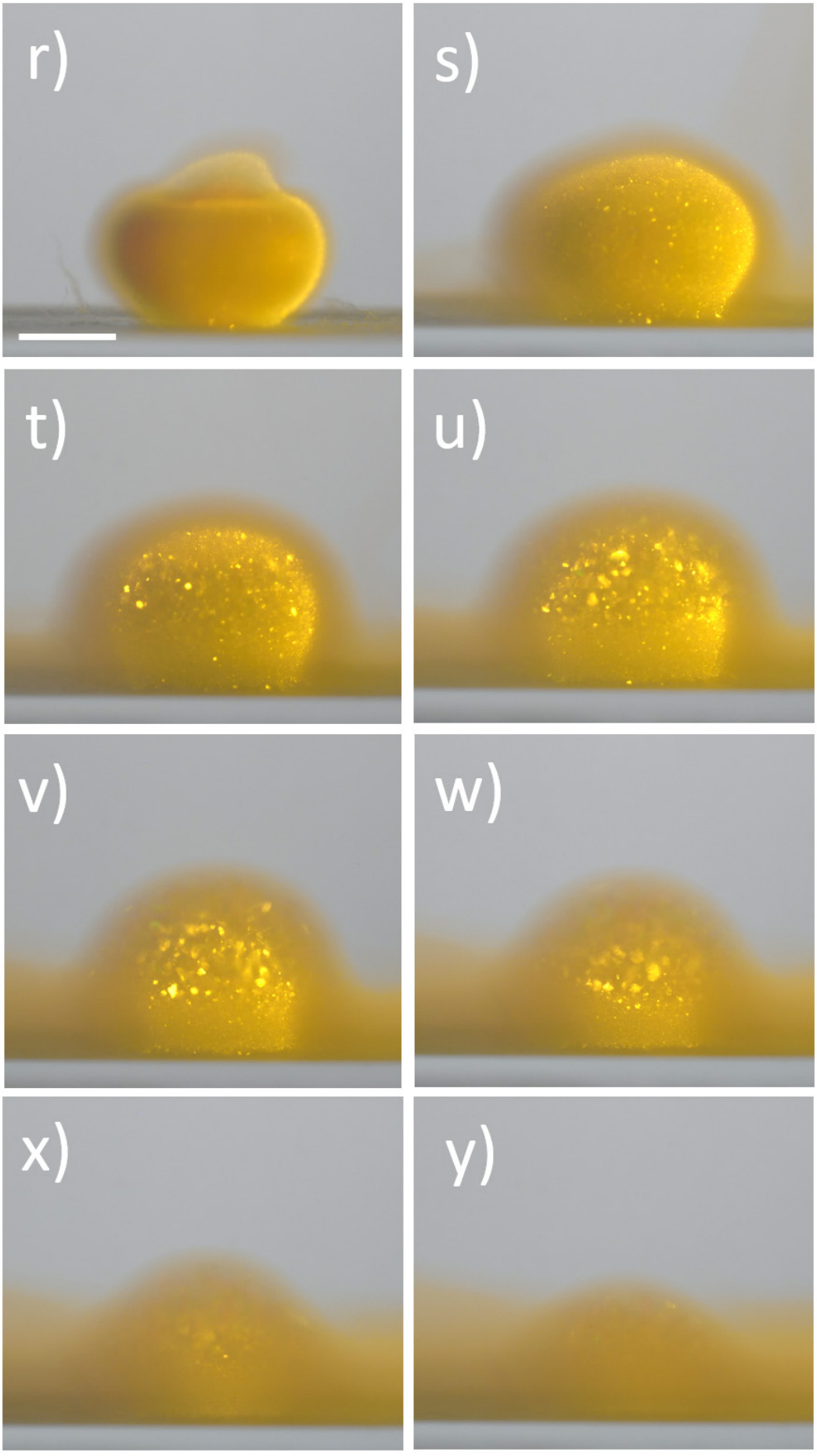
r)
s)
t)
u)
v)
w)
x)
y)

Fig. S9 Example time series for two drops observed in different modes. The Scale bars are 2mm. a)-h) Series of processed WB images of the drop shown in Fig. 2e. During processing, images were centred, aligned, white balance corrected for a colour temperature of 5000 K, cropped, and size calibrated. The scale bar is 2 mm. i)-q) MM image series for λ = 611 nm. Images were recorded at t = {60 s, 360 s, 660 s, 960 s, 1260 s, 1560 s, 1860 s, 2160 s} and processed after capture (centred, aligned, white balance corrected using a 5x5 pixel area of the background, cropped, and size calibrated). r)-y) The same but for λ = 590 nm.

Extracting wavelengths from WB images for density profiling

As mentioned in the main text, we attempted in WB imaging to extract the scattered wavelengths of (200) Bragg reflections from the corresponding RGB readings using a recently proposed approach [20]. It corrects for the hue dependence of the RGB readings by normalizing each channel to the total intensity, and it originally was applied to the analysis of changes in the dominant colour of Gecko skin. Applied to expanding crystals showing (200) scattering, however, it failed to produce reliable results. The main difference between the two experimental situations is the use of monochromatic sensor illumination by the Bragg reflections, which leads to a positioning of the provided sensor illumination outside the RGB triangle in the C.I.E. 1931 chromaticity diagram [21, 22]. We therefore tested our sensor for its reaction to this type of illumination. The light of a halogen lamp (Avalight-DH-S; LS-0610025, Avantes B.V., Apeldoorn, NL) was collimated, dimmed by a variably neutral filter and diffracted using a line grating. From the continuous 1st order diffraction pattern, a tiny spectral range ($\Delta\lambda \leq$ 0.8nm) was selected by a slit aperture and allowed to impinge on the CMOS sensor of the camera. The RGB readings are compared in Fig. S9a to the independently recorded spectrum of the lamp (AvaSpec-2048-SPU2-FC 286 nm-841 nm; Avantes B.V., Apeldoorn, NL). Under quasi single-wavelength illumination, significant secondary red and green maxima are observed in the sensor RGB readings short-side the main red and green maxima (arrows). These effects became more pronounced at increasing intensities. Applying the procedure suggested by [20] then yields a near linear but not strictly monotonous relation between observed and assigned wavelength. This is shown in Fig. S9b. In particular, the two regions between 520 nm and 570 nm and below 470nm are strongly affected, and no unequivocal wavelength identification is possible there. The tested approach thus renders assigned densities unreliable. To exclude an influence of the specific high resolution camera sensor of the D850, we also tested several other Nikon SLRs including the one used in [20](D700, D750, D800, and D810) consistently reproducing the effect of secondary maxima. We further analysed white light passing a diffusor screen instead of a grating. Quite remarkably, no pronounced secondary maxima in the RGB sensitivity were observed. Rather, this time the spectral shapes featured single maxima with monotonous rise and decay. Moreover, this behaviour was independent of intensity. We therefore suspect that the present failure of the approach in interpreting MM-images is related to the use of monochromatic light entering the camera and leading to issues with the hue calibration. In hindsight this might be less surprising, since the tested procedure was designed to work for illumination by light lying inside the RGB triangle, and not from the borders of the C.I.E. colour-space.

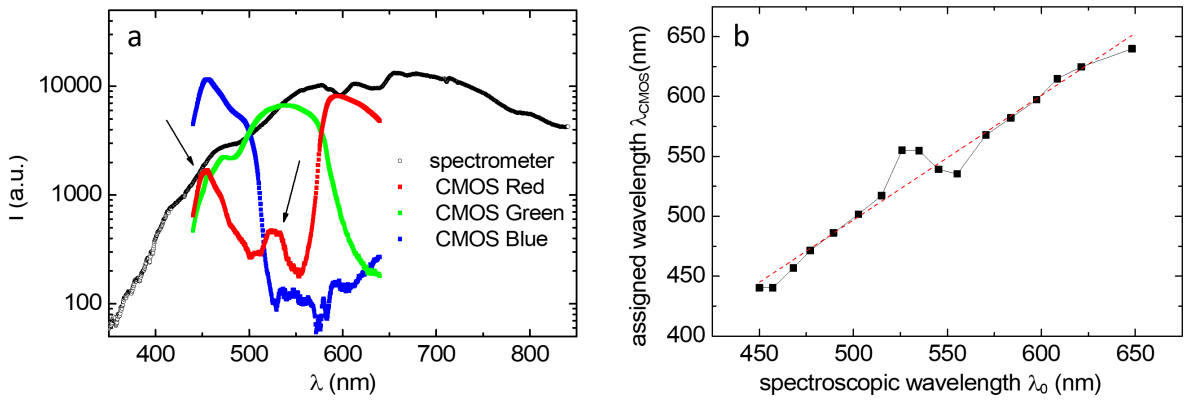

Fig. S10 Assignment of illuminating wavelengths to readout RGB values. a) Spectrum of the halogen lamp used for illumination in the experiments (black) compared to the corresponding CMOS readouts for the three colour channels R, G, and B, as recorded under single wavelength illumination. The arrows mark secondary maxima. b) Calibration curve resulting from evaluation of RGB readings with the procedure suggested by Teyssier et al. [20].

Additional information concerning model calculations

We studied the evolution of the central density in our DDFT calculations. We used the following (reduced) standard parameters to obtain and display the data shown in Fig. S10:

d = 80 nm

$D = 4D_0$ with $D_0 = k_B T/3\pi\eta d$

Z = 365

ρ_0 = 110 µm^{-3}

V_0 = 11.5 mm^3

η = 1 10^{-3} Pas

$a_0 = (2/\rho_0)^{1/3}$

$r_0 = 10^3 a_0$

$\kappa = 3a_0^{-1}$

$U = 10^3 k_B T a_0$.

The reduced time unit is $t = 10^3\ a_0^2 D$.

For very short times, the central density remains constant (see inset). It then decays in a slowing fashion. The latter is due to the gradual vanishing of the density gradient in the core centre. At long times, the drop core region thus shows a homogeneous and isotropic expansion.

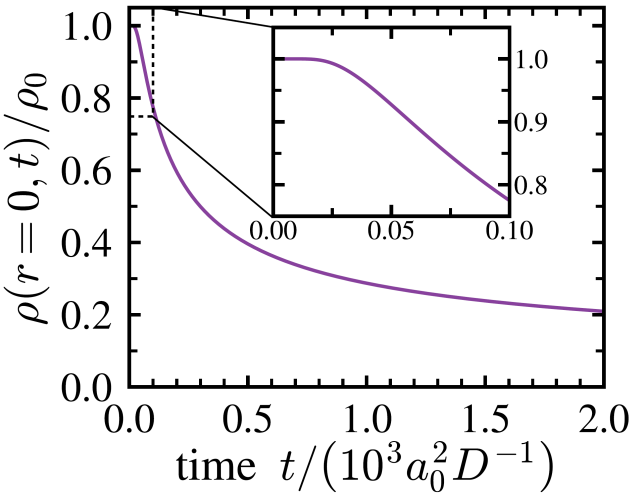

Fig. S11 Evolution of the central density in the model calculations. Shown is the result of model calculations using the above standard input parameters. The inset shows an enlargement of the initial core density evolution showing the minimally delayed onset of density reduction.

References

1 D. Hessinger, M. Evers, T. Palberg, *Phys. Rev. E* **61**, 5493-5506 (2000). **Independent Ion Migration in Suspensions of Strongly Interacting Charged Colloidal Spheres**

2 T . Palberg, H. Hecht, E. Simnacher, T. Loga, F. Falcoz, J. Kottal, P. Leiderer, *J. Phys. III (France)* **4**, 457-471 (1994). **Determination of the shear modulus of colloidal solids with high accuracy**

3 L. Shapran, H. J. Schöpe, T. Palberg, *J. Chem. Phys.* **125**, 194714 (2006). **Effective charges along the melting line of colloidal crystals**

4 P. Wette, H.-J. Schöpe, R. Biehl, T. Palberg, *J. Chem. Phys.* **114**, 7556-7562 (2001). **Conductivity of deionised two-component colloidal suspensions**

5 H.-J. Schöpe, T. Palberg, *J. Colloid Interface Sci.* **234**, 149-161 (2001). A multipurpose instrument to measure the vitreous properties of charged colloidal solids

6 T. Okubo, H. Ishiki, *J. Colloid Interface Sci.* **211**, 151-159 (1999). **Kinetic Analyses of Colloidal Crystallization in a Sinusoidal Electric Field as Studied by Reflection Spectroscopy**

7 R. Pike and P. Sabatier (Eds.), *Scattering* N. Y., Academic Press 2002.

8 P. Wette, H.-J. Schöpe T. Palberg, *Colloid Surf. A* **222**, 311-321 (2003). **Experimental Determination of Effective Charges in Aqueous Suspensions of Colloidal Spheres**

9 M. O. Robbins, K. Kremer, and G. S. Grest, *J. Chem. Phys.* **88**, 3286-3312 (1988). **Phase diagram and dynamics of Yukawa Systems**

10 S. Hamaguchi, R.T. Farouki, D.H.E. Dubin, *Phys. Rev. E* **56**, 4671-4682 (1997). **Triple point of Yukawa systems**

11 E. J. Meijer, D. Frenkel, *J. Chem. Phys.* **94**, 2269-2271 (1991). **Melting line of Yukawa system by computer simulation**

12 S. Alexander J. P. Mc Tague, *Phys. Rev Lett.* **41**, 702 (1978). **Should All Crystals Be bcc? Lan-dau Theory of Solidification and Crystal Nucleation**

13 W. Härtl, H. Versmold, *J. Chem. Phys.* **80**, 1387-1389 (1984). **An experimental verification of incoherent light scattering**

14 G. Nägele, *Phys. Reports* **272**, 215-372 (1996). **On the dynamics and structure of charge-stabilized suspensions**

15 T. Palberg, *J. Phys.: Condens. Matter* **11**, R323-R360 (1999). **Crystallisation kinetics of repulsive colloidal spheres**

16 P. N. Pusey, *Curr. Opn. Colloid Interface Sci.* **4**, 177-185 (1999). **Suppression of multiple scatter-ing by photon cross-correlation techniques**

17 R. J. Spry, D. J. Kosan, *Appl. Spectroscopy* **40**, 782-784 (1986). **Theoretical Analysis of the Crystalline Colloidal Array Filter**

18 D. Botin, L. Marota Mapa, H. Schweinfurth, B. Sieber, C. Wittenberg, T. Palberg, *J. Chem. Phys.* **146**, 204904 (2017). An Empirical Correction for Moderate Multiple Scattering in in Super-Heterodyne Light Scattering
19 J. L. Langford, A. J. C. Wilson, *J. Appl. Cryst.* **11**, 102-113 (1978). **Scherrer after Sixty Years: A Survey and Some New Results in the Determination of Crystallite Size**
20 J. Teyssier, S. V. Saenko, D. van der Marel, and M. C. Milinkovitch, Nature Comm. 6, 6368 (2015). **Photonic crystals cause active colour change in chameleons**
21 T. Smith, J- Gould, *Transactions of the Optical Society. **33,** 73–134 (1931–32).* doi:10.1088/1475-4878/33/3/301 **The C.I.E. colorimetric standards and their use**
22 J. Schanda, *Colorimetry: Understanding the CIE System*, Hoboken, John Wiley & Sons, 2007.